

Spatial Sensitivity Distribution of Surface Acoustic Wave Resonator Sensors

David A. Powell, *Member, IEEE*, Kourosh Kalantar-zadeh, *Member, IEEE*, and Wojtek Wlodarski, *Member, IEEE*

Abstract—The sensitivity distribution of surface acoustic wave (SAW) resonator sensors is investigated by theoretical and experimental means. It is shown that the sensitivity to mass loading varies strongly across the surface due to the confinement of acoustic energy toward the center of the device. A model is developed for this phenomenon based on the extraction of coupling of modes parameters from a rigorous boundary element method analysis based on a periodic Green's function. As SAW sensors for many applications include a layer covering the electrodes, a new technique is introduced to account for the mechanical interactions with buried electrodes. Using this technique, the sensitivity calculations are found to be in good agreement with measurements. It is also shown that while changes in other parameters influence sensitivity, it is velocity change that most strongly determines overall frequency change.

Index Terms—Boundary element method (BEM), layered, matrix eigen-operator, resonator, sensitivity, surface acoustic wave (SAW).

I. INTRODUCTION

SURFACE acoustic wave (SAW) sensors are well established for sensing applications [1]. For applications in liquid media, shear horizontal modes are used since they minimize loss of acoustic energy into the liquid [2]. Compared to SAW devices based on a delay-line configuration, resonator structures offer higher frequency stability for a given device size due to the multiple reflections increasing the group delay. A schematic layout of a two-port SAW resonator structure is shown in Fig. 1, where it should be noted that the number of electrodes is actually much greater. Propagation is in the x_1 -direction, and the device surface is normal to the x_3 -direction.

Regions B–C and D–E represent the input and output interdigital transducers (IDTs) that are connected to the external circuit. Regions A–B and E–F are short-circuited electrode gratings of the same period as the IDTs. These electrode gratings reflect acoustic energy at acoustic wavelengths close to the period of the electrodes, thus forming a resonant cavity. Region C–D is a grating with a different period to that of the IDTs. It is required for some shear horizontal modes to ensure confinement of acoustic energy to the surface without causing significant reflection. The grating also ensures that acoustic energy confinement toward the surface is consistent across the

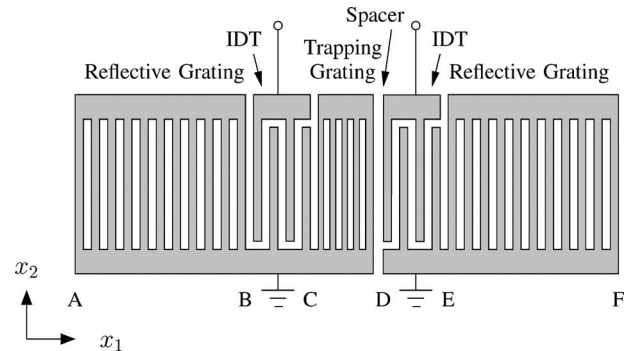


Fig. 1. Layout of two-port resonator SAW sensor in (x_1, x_2) plane.

device. This means that variations in sensitivity across the device surface due to lack of metallization will not occur. There is a small gap at point D that gives fine control over the location of the resonant frequency.

SAW transducer sensitivity has been investigated by both theoretical and experimental means (e.g., [3]–[5]). However, the approach taken in all theoretical work so far has been to consider a uniform homogeneous film that covers the entire surface of an infinite-sized device. The authors previously established that the mass sensitivity differs for free surface, metallized surface, and an electrode array [6], particularly for highly piezoelectric materials. It has also been reported that most of the sensitivity of a SAW resonator can be attributed to a small region at the center [7], and that a sample delivery system that concentrates the analyte on this small region in the center can improve the overall sensitivity of the system [8]. However, no quantitative analysis was performed to characterize the sensitivity variation across the surface. More recently, the authors have theoretically and experimentally quantified this effect [9]. The variation is much greater than that previously reported over the surface of a delay-line SAW sensor [10], which differs predominantly between the electrode regions and the delay path.

In this paper, the mass sensitivity variation over the surface of a resonator will be further investigated by both theoretical and experimental means. The boundary element method (BEM) extensions necessary to achieve good agreement between theory and experiment will be explained in detail. The BEM model is used here to calculate parameters for the coupling of modes (COM) model, which has previously been applied to the design of SH-SAW resonators for liquid media biosensing applications [11]. The COM model is then used to develop a P-matrix description of the structure, which can then be used to study the variation of sensitivity across the device surface.

Manuscript received March 14, 2006; revised June 2, 2006. The associate editor coordinating the review of this paper and approving it for publication was Prof. Fabien Josse.

The authors are with the School of Electrical and Computer Engineering, RMIT University, Melbourne, Vic. 3001, Australia (e-mail: david.powell@ieee.org; kourosh.kalantar@rmit.edu.au; ww@rmit.edu.au).

Digital Object Identifier 10.1109/JSEN.2006.882779

The implications of this surface sensitivity variation are particularly important in cases where only a small quantity of selective material is available, so that it can be placed on the most sensitive region of the SAW device. Similar considerations also apply when a limited amount of analyte is available. For example, in immuno-sensing applications, expensive antibodies or antigens are immobilized onto the device surface. By the use of a resonator structure with carefully selected sensitive region, greater response could be observed. In addition, the resonator may be designed in order to tailor the sensitivity distribution to suit a sample delivery system.

II. MODEL

The model used here is based on the formulation of a spectral domain Green's function $\bar{G}(k_1)$ that describes the acoustic wave properties of the substrate and guiding layer under the two-dimensional (2-D) approximation. This can be calculated using well-known techniques [12], [13] and may also be extended to layered structures [14], [15]. The Green's function relates displacement $\bar{\mathbf{u}}$ and voltage $\bar{\varphi}$ to sources of surface-normal stress $\bar{\boldsymbol{\tau}}$ and charge \bar{q} . The relationship is simplest and most useful in the spectral (wavenumber) domain, i.e.,

$$\begin{bmatrix} \bar{\mathbf{u}} \\ \bar{\varphi} \end{bmatrix} = \begin{bmatrix} \bar{G}_{u\tau} & \bar{G}_{uq} \\ \bar{G}_{\varphi\tau} & \bar{G}_{\varphi q} \end{bmatrix} \begin{bmatrix} \bar{\boldsymbol{\tau}} \\ \bar{q} \end{bmatrix}. \quad (1)$$

It is convenient to define a surface impedance $\bar{Z}(k_1) = \bar{G}(k_1)^{-1}$, which can be partitioned in a similar fashion. Since the devices have a large number of electrodes, a periodic Green's function analysis is used to reduce the computation time. In a system with period p in the x_1 -direction, Floquet's theorem dictates that the field quantities obey the relationship [16]

$$\psi(x_1) = \psi(x_1 + np) \exp(j\beta np) \quad (2)$$

where n is an integer, β is a phase shift between periods, and ψ is a vector of all field variables appearing in (1).

A. Thin Electrode Approximation

If the mechanical sources are neglected, then only the Green's function term $\bar{G}_{\varphi q}$ needs to be considered, which further reduces computation time. Using normalized pulses of width w as weighting and basis functions, the following equation relates voltage on subregion n of the electrode to charge on subregion m of the electrode:

$$\varphi_n(\beta, \omega) = \frac{1}{p} \sum_{l=-L}^L \bar{G}_{\varphi q}(\beta_l, \omega) \sum_{m=1}^M \frac{\sin(\beta_l w_m)}{\beta_l w_m} \times \frac{\sin(\beta_l w_n)}{\beta_l w_n} e^{j\beta_l(x_n - x_m)} q_m(\beta, \omega) \quad (3)$$

where $\beta_l = \beta + lQ$, M is the number of pulse functions, $Q = 2\pi/p$ is the synchronous wavenumber of the electrode array, and $2L + 1$ is the number of harmonics of the Green's function used. By specifying the electrode voltage and solving for the

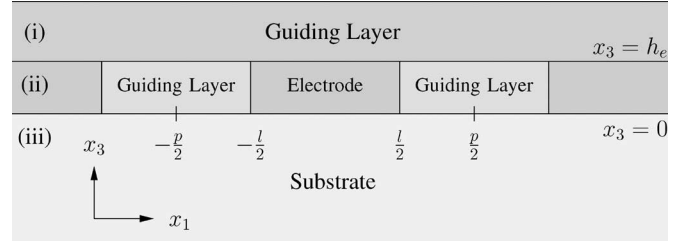


Fig. 2. Basic periodic structure to be modeled.

charge distribution, the harmonic admittance of the structure can be calculated [17]. This analysis is sufficiently accurate only if it can be assumed that mechanical interactions between the electrodes and the acoustic wave are negligible.

B. Full Electrode Model

In order to improve accuracy in cases where the height or mass of the electrodes makes a significant contribution to the device performance, a method that includes these effects must be utilized. Typically, the finite element method (FEM) is used to account for such interactions [18], [19]; however, FEM becomes cumbersome and requires a high-element density in the case of electrodes embedded within layered media [20]. Since the problem with electrodes sandwiched between the substrate and the guiding layer is quite different from the well-known problem of electrodes upon the device surface, a new technique developed by the authors is presented here based on the formulation of a matrix eigen-operator [21].

By assuming that the electrode shape is perfectly rectangular, the problem is greatly simplified. This is because within the electrode region, there is no x_3 dependence of the material constants. The assumption that charge is restricted to the reference plane $x_3 = 0$ is retained for simplicity.

Referring to Fig. 2, the aim is to create a model for region (ii) since wave propagation in regions (i) and (iii) can already be accounted for in the existing Green's function model. This new model will take the form of a matrix relating the value of stress and displacement at $x_3 = 0$ (substrate surface) to that at $x_3 = h_e$. This matrix will then be incorporated into the periodic model.

The following matrix-operator form is used to describe the variation of field variables in the x_3 -direction [21]:

$$\begin{bmatrix} \mathcal{L}_{11} & \mathcal{L}_{12} \\ \mathcal{L}_{21} & \mathcal{L}_{22} \end{bmatrix} \begin{bmatrix} \bar{\mathbf{u}} \\ \bar{\varphi} \\ \bar{\boldsymbol{\tau}} \end{bmatrix} = \frac{\partial}{\partial x_3} \begin{bmatrix} \bar{\mathbf{u}} \\ \bar{\varphi} \\ \bar{\boldsymbol{\tau}} \end{bmatrix} \begin{bmatrix} \bar{\mathbf{u}} \\ \bar{\varphi} \\ \bar{\boldsymbol{\tau}} \end{bmatrix} \quad (4)$$

where the elements of operator \mathcal{L} have the form

$$\mathcal{L}_{11} = \mathcal{M}^{11} \frac{\partial}{\partial x_1} \quad (5a)$$

$$\mathcal{L}_{12} = \mathcal{M}^{12} \quad (5b)$$

$$\mathcal{L}_{21} = -\rho\omega^2 - \frac{\partial}{\partial x_1} \mathcal{M}^{21} \frac{\partial}{\partial x_1} \quad (5c)$$

$$\mathcal{L}_{22} = -\frac{\partial}{\partial x_1} \mathcal{M}^{22}. \quad (5d)$$

The matrices \mathcal{M}^{kl} and $\underline{\rho}$ are combinations of the material constants and the generalized density matrix, respectively, the values of which can be found by comparison with the equations presented in [21] or [14]. The novelty of the proposed technique lies in allowing these material constants to vary periodically with x_1 using a Fourier expansion

$$\mathcal{M}^{kl}(x_1) = \sum_{n=-\infty}^{\infty} \mathcal{M}_n^{kl} e^{jnQx_1} \quad (6)$$

$$\underline{\rho}(x_1) = \sum_{n=-\infty}^{\infty} \underline{\rho}_n e^{jnQx_1}. \quad (7)$$

Referring to Fig. 2, the region $-l/2 < x_1 < l/2$ of each period in region (ii) is considered to consist of the electrode material; the remainder to consist of the guiding layer material.

For the field variables $\psi(x_1, x_3)$, the Floquet solution given in (2) applies. In this case, the value of the field variables must be considered throughout the range $0 < x_3 < h_e$ rather than only at $x_3 = 0$ as for the thin electrode model. Again, a phase-shifted Fourier series representation is used as

$$\psi(x_1, x_3, \beta, \omega) = \sum_{n=-\infty}^{\infty} \psi_n(x_3, \beta, \omega) \exp(jnQx_1) \exp(j\beta x_1). \quad (8)$$

The x_3 dependency can be accounted for by making the substitution

$$\psi_n(x_3, \beta, \omega) = \psi_n(0, \beta, \omega) \exp(-jk_3(\beta, \omega)x_3). \quad (9)$$

At this stage, it will be convenient to consider only the nonpiezoelectric case, which decouples the electrical and mechanical solutions. Substituting (8) and (9) into the eigenoperator (4) and truncating the Fourier series representations to the range from $[-N, N]$, an algebraic form L results as

$$\sum_{n=-N}^N \begin{bmatrix} L_{mn}^{11} & L_{mn}^{12} \\ L_{mn}^{21} & L_{mn}^{22} \end{bmatrix} \begin{bmatrix} \bar{\mathbf{u}}_n \\ \bar{\boldsymbol{\tau}}_n \end{bmatrix} = (-jk_3) \begin{bmatrix} \bar{\mathbf{u}}_m \\ \bar{\boldsymbol{\tau}}_m \end{bmatrix} \quad (10)$$

with

$$L_{mn}^{11} = -(j\beta_n) \mathcal{M}_{m-n}^{11} \quad (11a)$$

$$L_{mn}^{12} = \mathcal{M}_{m-n}^{12} \quad (11b)$$

$$L_{mn}^{21} = -\omega^2 \rho_{m-n} + (\beta_n(m-n)Q + \beta_n^2) \mathcal{M}_{m-n}^{21} \quad (11c)$$

$$L_{mn}^{22} = (-j(m-n)Q - j\beta_n) \mathcal{M}_{m-n}^{22}. \quad (11d)$$

By solving the algebraic eigenvalue problem, a mechanical transmission matrix can be defined for the inhomogeneous

layer as

$$\begin{bmatrix} \bar{\mathbf{u}}(x_3, \beta, \omega) \\ \bar{\boldsymbol{\tau}}(x_3, \beta, \omega) \end{bmatrix} = \Phi^{\text{mech}}(\beta, \omega, h_e) \begin{bmatrix} \bar{\mathbf{u}}(x_3 + h_e, \beta, \omega) \\ \bar{\boldsymbol{\tau}}(x_3 + h_e, \beta, \omega) \end{bmatrix} \quad (12)$$

where

$$\Phi^{\text{mech}}(\beta, \omega, h_e) = \exp(-Lh_e). \quad (13)$$

In addition, there is also an electrical transmission matrix

$$\begin{bmatrix} \bar{\varphi}(x_3, \beta, \omega) \\ \bar{D}_3(x_3, \beta, \omega) \end{bmatrix} = \Phi^{\text{elec}}(\beta, \omega, h_e) \begin{bmatrix} \bar{\varphi}(x_3 + h_e, \beta, \omega) \\ \bar{D}_3(x_3 + h_e, \beta, \omega) \end{bmatrix}. \quad (14)$$

For simplicity, the electrical transmission matrix is treated as being through homogeneous isotropic media, which gives the analytical solution in (15) and (16), shown at the bottom of the page.

The inhomogeneous nature of the layer containing buried electrodes means that a relationship of the following form exists:

$$\bar{\varphi}(\beta + kQ, \omega) = \sum_l \bar{G}_{kl}(\beta, \omega) \bar{q}(\beta + lQ, \omega) \quad (17)$$

$$\bar{\varphi}_k(\beta, \omega) = \sum_l \bar{G}_{kl}(\beta, \omega) \bar{q}_l(\beta, \omega). \quad (18)$$

The matrix containing these elements shall be denoted as $\mathcal{G}(\beta, \omega)$, the multispectral Green's function, and as with the spectral domain Green's function, it has an inverse $\mathcal{Z}(\beta, \omega)$. A homogeneous medium can be included within this formulation by making the substitution

$$\bar{G}_{kl} = \delta_{kl} \bar{G}(\beta + lQ, \omega). \quad (19)$$

Referring to Fig. 2, the substrate and homogeneous layer can be described by this means and will be represented by multispectral impedance matrices $\mathcal{Z}^{(iii)}$ and $\mathcal{Z}^{(i)}$, respectively. If Φ^{mech} and Φ^{elec} are partitioned and combined, we get

$$\begin{bmatrix} \bar{\mathbf{u}}_k(x_3) \\ \bar{\varphi}_k(x_3) \\ \bar{\boldsymbol{\tau}}_k(x_3) \\ \bar{D}_{3,k}(x_3) \end{bmatrix} = \sum_l \begin{bmatrix} \Phi_{kl}^{uu} & 0 & \Phi_{kl}^{u\tau} & 0 \\ 0 & \Phi_{kl}^{\varphi\varphi} & 0 & \Phi_{kl}^{\varphi D} \\ \Phi_{kl}^{\tau u} & 0 & \Phi_{kl}^{\tau\tau} & 0 \\ 0 & \Phi_{kl}^{D\varphi} & 0 & \Phi_{kl}^{DD} \end{bmatrix} \times \begin{bmatrix} \bar{\mathbf{u}}_l(x_3 + h_e) \\ \bar{\varphi}_l(x_3 + h_e) \\ \bar{\boldsymbol{\tau}}_l(x_3 + h_e) \\ \bar{D}_{3,l}(x_3 + h_e) \end{bmatrix} \quad (20)$$

where the subscripts k and l refer to the harmonic number.

It should be noted that this procedure can also be performed for the full anisotropic and piezoelectric case, which results in

$$\Phi^{\text{elec}}(\beta, h_e) = \begin{bmatrix} \Phi^{\varphi\varphi} & \Phi^{\varphi D} \\ \Phi^{D\varphi} & \Phi^{DD} \end{bmatrix} \quad (15)$$

$$= \delta_{nm} \begin{bmatrix} \cosh[(\beta + nQ)h_e] & \frac{1}{(\beta + nQ)\varepsilon} \sinh[(\beta + nQ)h_e] \\ (\beta + nQ)\varepsilon \sinh[(\beta + nQ)h_e] & \cosh[(\beta + nQ)h_e] \end{bmatrix} \quad (16)$$

a similar formulation and longer computation time. This can be regarded as a generalization of Adler's [14] chain matrix technique for layered media, extended to the case where the material constants are a function of x_1 . Combining (20) with $\mathcal{Z}^{(i)}(\beta, \omega)$, the impedance matrix of the region above the reference plane $\mathcal{Z}^{(a)}(\beta, \omega)$ is calculated from

$$\mathcal{Z}^{(a)} = \left(\begin{bmatrix} \Phi^{\tau u} & 0 \\ 0 & \Phi^{D\varphi} \end{bmatrix} + \begin{bmatrix} \Phi^{\tau\tau} & 0 \\ 0 & \Phi^{DD} \end{bmatrix} \mathcal{Z}^{(i)} \right) \times \left(\begin{bmatrix} \Phi^{uu} & 0 \\ 0 & \Phi^{\varphi\varphi} \end{bmatrix} + \begin{bmatrix} \Phi^{u\tau} & 0 \\ 0 & \Phi^{\varphi D} \end{bmatrix} \mathcal{Z}^{(i)} \right)^{-1}. \quad (21)$$

The multispectral impedance matrix of the complete structure can now be calculated by

$$\mathcal{Z}(\beta, \omega) = \left(\mathcal{Z}^{(a)}(\beta, \omega) - \mathcal{Z}^{(iii)}(\beta, \omega) \right). \quad (22)$$

Since all mechanical interactions are already included within this formulation, the problem can be reduced to a purely electrical one. The multispectral electrical Green's function can be calculated as

$$\mathcal{G}^{\varphi q}(\beta, \omega) = \left(\mathcal{Z}^{q\varphi} - \mathcal{Z}^{qu}(\mathcal{Z}^{\tau u})^{-1} \mathcal{Z}^{\tau\varphi} \right)^{-1}. \quad (23)$$

Utilizing the method of weighted residuals and following a similar procedure to that used for the simplified electrical Green's function model, the resulting matrix equation is

$$\varphi_n(\beta, \omega) = \frac{1}{p} \sum_{k=-L}^L e^{j\beta_k x_n} \frac{\sin(\beta_k w_n)}{\beta_k w_n} \sum_{l=-L}^L \bar{G}_{kl}(\beta, \omega) \times \sum_{m=-N}^N e^{-j\beta_l x_m} \frac{\sin(\beta_l w_m)}{\beta_l w_m} q_m(\beta, \omega). \quad (24)$$

This can then be used to calculate the charge distribution, thus yielding the harmonic admittance function $Y(\beta, \omega)$. This function gives the admittance per electrode of the infinite array, and by locating its singularities, the dispersion curve for the structure may be obtained.

C. Calculation of Frequency Response

Regardless of whether the thin electrode simplification or the full mechanical model is used, the result of the Green's function-based BEM analysis is a harmonic admittance function. A fitting procedure [22] is used to derive COM parameters from this function without requiring the complete dispersion curve. The COM model has parameters for propagation velocity v , reflection κ , transduction α , capacitance C , and attenuation γ . Being a phenomenological model, it is able to model the device frequency response with low computational cost but requires that its parameters be derived from measurement or from more rigorous simulation. This approach is advantageous because it combines the speed and simplicity of the COM model with the accuracy of the rigorous BEM solution. The application of this combination of models to layered SAW resonators operating in liquid media was previously reported in [6].

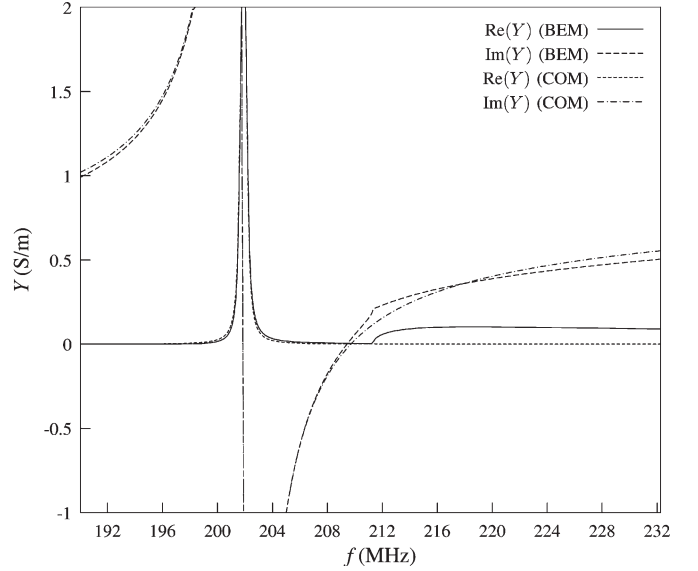


Fig. 3. Comparison of harmonic admittance calculated from BEM and fitted to COM parameters.

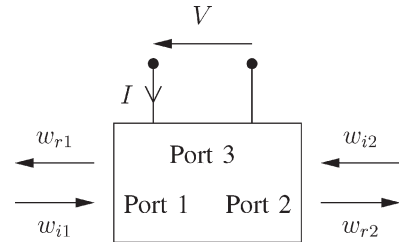


Fig. 4. P-matrix basic block.

This approach can be applied to both Rayleigh and (pure or quasi) shear-horizontal modes. The accuracy of the COM model in the case of shear-horizontal waves is not as good as for Rayleigh waves as bulk wave generation can occur at frequencies near or even within the stopband [23]. Since the primary quantity of interest here is the resonant frequency, the COM model can be applied so long as the resonant frequency of the device occurs below the bulk-wave cutoff frequency. This can be verified by examining the harmonic admittance curve (as shown in Fig. 3). The values calculated by the BEM model and those fitted by the COM model are shown, showing that the fit is good apart from some minor dispersion effects and the bulk-wave generation. It should be noted that depending on the device design, the resonant frequency may be different from that of the infinite array, and it is the device's resonant frequency that must be compared with the bulk-wave cutoff frequency.

Referring to Fig. 4, a P-matrix is a three-port description relating voltage, current, and acoustic wave amplitude, i.e.,

$$\begin{bmatrix} w_{r1} \\ w_{r2} \\ I \end{bmatrix} = \begin{bmatrix} P_{11} & P_{12} & P_{13} \\ P_{21} & P_{22} & P_{23} \\ P_{31} & P_{32} & P_{33} \end{bmatrix} \begin{bmatrix} w_{i1} \\ w_{i2} \\ V \end{bmatrix} \quad (25)$$

where w_i are the incident acoustic wave amplitudes at ports 1 and 2, V is the bus-bar voltage, w_r are the reflected acoustic wave amplitudes at each port, and I is the bus-bar current. A P-matrix is created for each homogeneous section of the

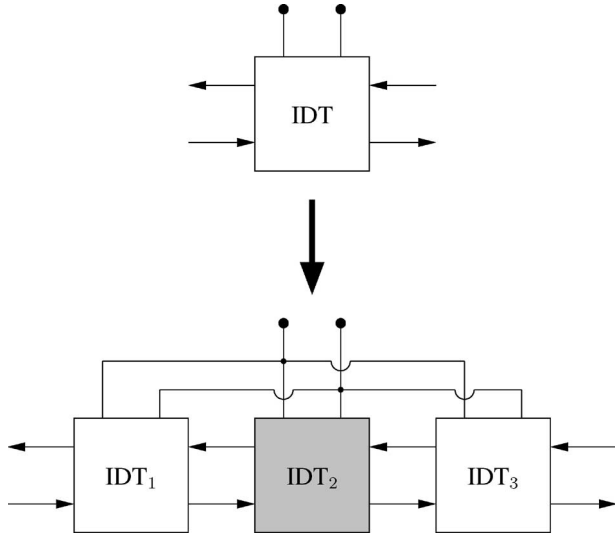


Fig. 5. Partitioning of P-matrix elements to include inhomogeneous mass loading.

device, such as an IDT, short circuit grating, or gap. For structures other than IDTs, port 3 does not exist; thus, the P-matrix will be 2×2 for electrode gratings and gaps. The value of P-matrix elements can be determined directly from the COM parameters, number of electrodes, and aperture width according to the equations given in [17].

This approach needs to be modified to take into account the mass loading of specific regions of the device. Consider Fig. 5, where the equivalent network of the IDT is replaced by three networks IDT₁, IDT₂, and IDT₃ with their acoustic ports cascaded and their electrical ports in parallel. Network IDT₂ represents the region subject to mass loading.

To implement this model, the COM parameters are calculated separately for the case with and without mass loading. These COM parameters can be used to create P-matrices of the subelements of the IDT; however, it was discovered that direct implementation of this procedure can produce spurious results. If the operation described by Fig. 5 is implemented with network IDT₂ having the COM parameters for the nonmass-loaded case, then it would be expected that the combined network would be identical to the original network. In fact, it was found that some slight difference occurred. To eliminate these effects, the P-matrix was calculated for a single electrode pair, both with and without mass loading. These were then cascaded analytically using the expressions given in [24] to form networks IDT₁, IDT₂, and IDT₃. Since the IDT is always split into the maximum number of P-matrices, no further error can occur due to the splitting of IDT networks into subnetworks.

Mass sensitivity is calculated along the length (x_1) of the device. Variation of the mass sensitivity across the width (x_2) of the device has been neglected in this model. This can be assumed to be a second-order effect since the device geometry is constant across its width, which is $17.5\lambda_0$.

Using the P-matrix model, the complete two-port parameters of the SAW device can be calculated, and the resonant frequency f_r can be determined. For the device with no mass loading, the resonant frequency was determined by finding the maximum amplitude of the transfer characteristic S_{21} . At this

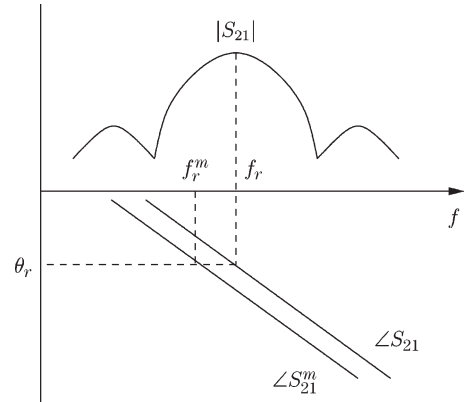


Fig. 6. Determination of device response when modeling mass loading.

frequency, the phase response will have a corresponding value of θ_r . When the device is subject to mass loading, the transfer response will change to S_{21}^m . The perturbed resonant frequency f_r^m is determined from the frequency where the phase response is θ_r , as illustrated in Fig. 6. It should be noted that the perturbed resonant frequency f_r^m does not necessarily correspond to the maximum magnitude of the perturbed transmission response S_{21}^m . This model is an idealization of the response of a SAW sensor when placed in a feedback loop to create an oscillator circuit.

For each region of the device, mass sensitivity is defined as

$$S_m^f = \frac{f_r^m - f_r}{m} \quad (26)$$

where m is the total mass of the perturbing material. This differs from the definition given in the literature (e.g., [4])

$$S_m^f = \frac{(f_r^m - f_r)/f_r}{m/a} \quad (27)$$

where a is the surface area. The change due to a finite mass is quantified in (26) and is expressed in terms of absolute, rather than relative, frequency change. This is a more appropriate measure since, in this paper, calculations are being made of finite regions of a device, rather than for an idealized infinite case, and the unperturbed resonant frequency is ideally equal in all cases. This results in an expression with SI units of hertz per kilogram; however, it is more practical to express it in units of hertz per nanogram.

III. MEASUREMENTS

The two-port resonator sensors were fabricated on a 36° -YX LiTaO₃ substrate. Gold electrodes of $0.1\text{-}\mu\text{m}$ thickness were patterned, the period of the IDT electrodes was $20\ \mu\text{m}$, and the aperture width was $350\ \mu\text{m}$. A $0.4\text{-}\mu\text{m}$ layer of SiO₂ was deposited on the device surface by RF magnetron sputtering. The resultant devices had resonant frequencies in the range of 205–206 MHz. It should be noted that for many sensing applications, a thicker layer would be used; however, a thinner layer was chosen because it reduces the impact of deposition process variation on the device performance. A SiO₂ guiding

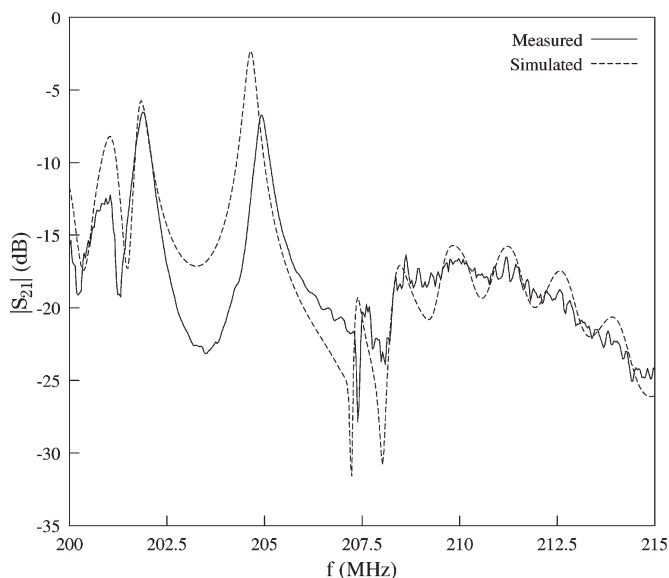


Fig. 7. Measured and calculated transmission response $|S_{21}|$.

layer was chosen instead of a polymer because its surface can be easily cleaned with relatively little damage to the layer. The measured and modeled S-parameters of the device are shown in Fig. 7, where the influence of the measurement jig has been included in the modeled results. It can be seen that the agreement is acceptable; however, bulk-wave generation effects are not included in the model, and there is some additional attenuation in the measured results.

Sensitivity measurements were performed by placing the SAW devices within the oscillator circuit before and after the addition of a perturbing mass and by measuring the change in oscillation frequency. The system was designed to ensure that the pressure placed on the SAW device by measurement probes was repeatable. The added mass was an AZ5206E photo-resist of thickness $0.6 \mu\text{m}$. This relatively thick layer was chosen to ensure that a strong response was observed. Because the photo-resist is a soft material, the velocity change should be mainly attributable to its mass. However, as the material is viscoelastic, additional attenuation is expected as well as some second-order influence on other device parameters. All measurements were carried out in air, as this greatly simplifies the task of placing a known quantity of material at a specified location. Each measurement was repeated simultaneously on five different devices, which were fabricated in the same batch.

Fig. 8 shows the measured mass sensitivity distribution. The horizontal axis of the graph gives the location along the x_1 -axis, as shown in Fig. 1, with the corresponding points A through F being marked out. Each horizontal line represents the region over which the additional mass has been deposited. The nearby crosses represent the measured values of sensitivity, and the circles give the average values of the measurements. In all cases, the mass has been deposited over the complete width of the device in the x_2 -direction.

These measurements show how a local change in mass loading at a region on the device surface affects the resonant frequency of the device. The sensitivity is negative because mass loading reduces the resonant frequency.

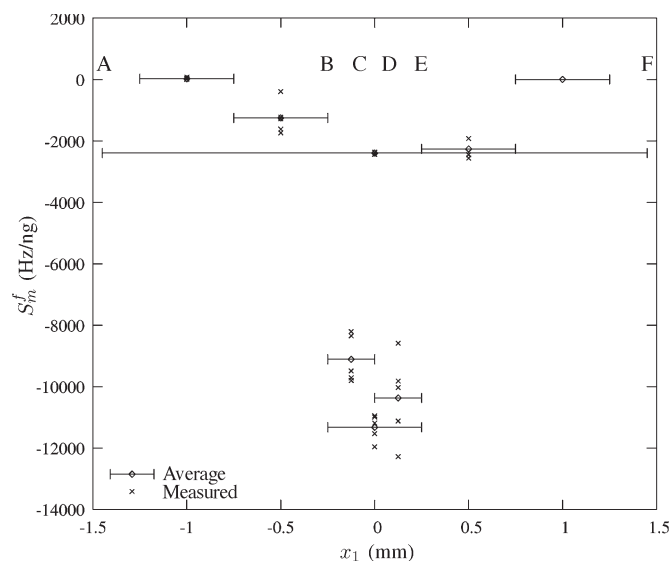


Fig. 8. Measured sensitivity distribution. The horizontal bars represent the region of the device over which the mass was deposited. Crosses represent the measurement values, and circles represent the average of these measurements.

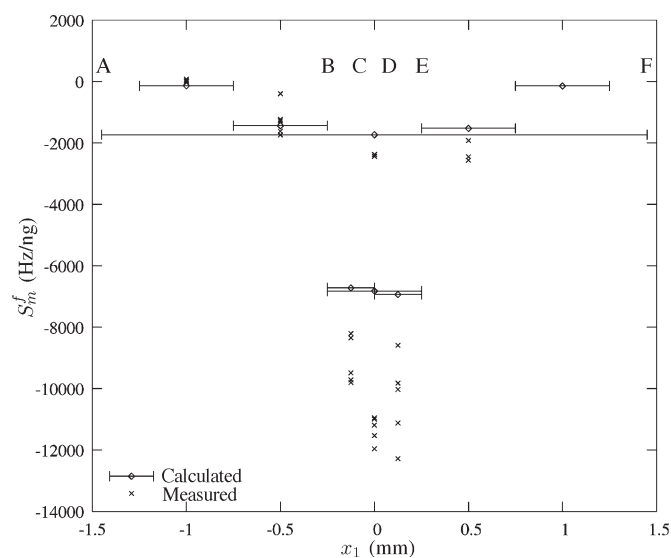


Fig. 9. Sensitivity distribution with thin electrode model. The horizontal bars represent the region of the device over which the mass was deposited. Crosses represent the measurement values, and circles represent the calculated values.

IV. COMPARISON OF MEASURED AND CALCULATED SENSITIVITY

A. Thin Electrode Approximation

Provided that the electrodes are of negligible thickness compared with the acoustic wavelength and are made from a light material, their mechanical properties do not need to be taken into account, and they can be considered as being infinitely thin. This assumption greatly simplifies the analysis and speeds up the computation. Fig. 9 shows the theoretical sensitivity using the model described in Section II-A and compares it with measurements. The measured values are represented by crosses, while the theoretical values are represented by the circles at the center of the horizontal bars. It can be seen that, as expected, the sensitivity is greatest at the center of the device. The region

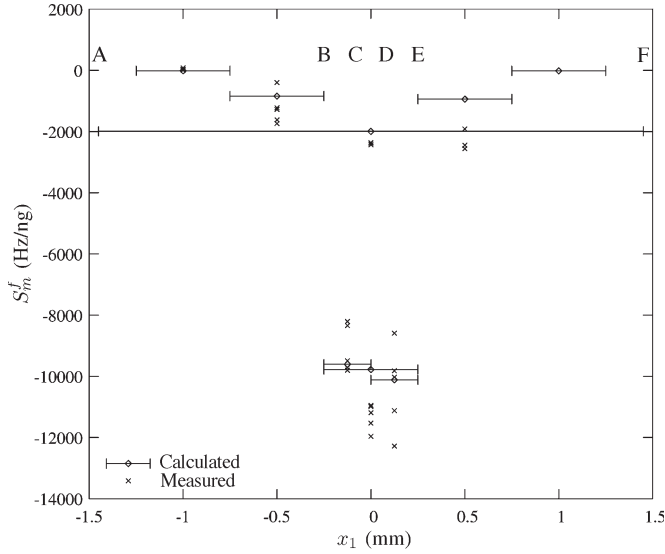


Fig. 10. Sensitivity distribution with full electrode model. The horizontal bars represent the region of the device over which the mass was deposited. Crosses represent the measurement values, and circles represent the calculated values.

B–E will be denoted the optimum region, although this region is arbitrarily selected and may be chosen differently for another device geometry. This region accounts for the majority of the total device response.

The qualitative agreement in shape is quite good; however, the measured sensitivity is more confined to the center than the model predicts, and the average sensitivity over the complete device is also greater. This disagreement can be attributed to the mechanical influence of the electrodes that was not included in the model. The heavy electrodes enhance the acoustic reflection, thus confining the acoustic energy to the center of the device. They also trap acoustic energy to the surface, thus further increasing the average mass sensitivity of the device.

B. Full Electrode Model

The results in Section IV-A indicate that mechanical electrode interactions have a significant influence on the performance of the device. To improve the agreement between the calculated and experimental results, the novel model developed in Section II-B was applied to the problem.

With the mechanical electrode model incorporated into the periodic Green's function analysis, the sensitivity was calculated as before. The results are shown in Fig. 10. The sensitivity shows better agreement with measurements in the case where complete device is mass loaded, as does the sensitivity in the optimum region. It can be seen that there is an asymmetry in the calculated sensitivity distribution. This is caused by the small gap at location D, which means that the structure and the acoustic energy distribution are both no longer symmetrical. Because the SiO₂ film is deposited conformally over a surface covered with electrodes, the top surface of the device has corrugations, which would also need to be included in the model for improved accuracy.

The change in velocity v is generally considered to be responsible for the frequency response due to mass loading, since for the region of a delay line between electrodes it is the

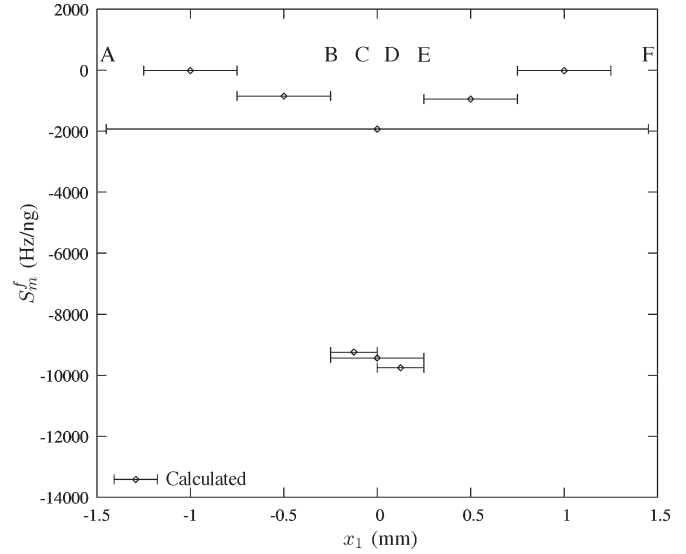


Fig. 11. Sensitivity distribution considering only velocity change.

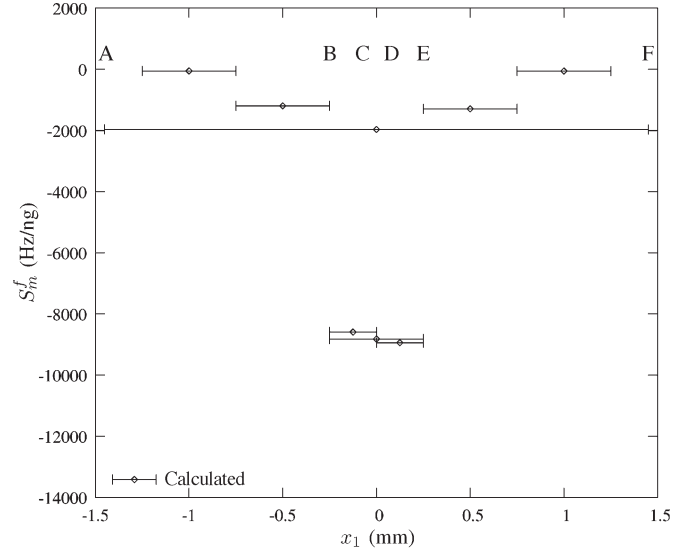


Fig. 12. Sensitivity distribution when subject to liquid loading.

only important parameter. However, since the COM parameters α , κ , C , and γ influence the frequency response of a resonator, a change in these parameters may be contributing to the results presented in Fig. 10. To determine the relative importance of velocity in determining sensitivity compared to these other parameters, all parameters except velocity have been held constant during mass loading. The resulting sensitivity distribution is shown in Fig. 11. It can be seen that the results do not differ greatly from those in Fig. 10, which indicates that in this case, the velocity change is predominant.

An important consideration is the influence of liquid media on the sensitivity distribution. Fig. 12 shows the calculated sensitivity distribution when there is a semi-infinite water layer above the device. It can be seen that the average sensitivity across the entire device does not differ significantly from the air-loaded case, although this does not take into account structural properties of the analyte, which may cause a change in sensitivity due to the degree of wave penetration into the liquid

TABLE I
SENSITIVITY COMPARISON

Structure	Sensitivity cm^2/g
Infinite Electrode Array	-114.3
Complete Resonator	-99.3
Optimum Region	-83.5

[25]. More significant is that the sensitivity is not as strong in the center. This can be attributed to the reduction of reflection coefficient for liquid loaded resonators with thin guiding layers, which was previously reported in [6]. This causes the acoustic energy to be less confined to the center.

V. DISCUSSION

It is of interest to compare the sensitivity of the complete device (A–F), of the optimum region (B–E), and of an idealized infinite length IDT, which is equivalent to the results of other methods that do not account for inhomogeneous loading. Table I shows a comparison of these sensitivity calculations. To compare with an infinite electrode array, mass loading per unit area must be considered. This shows that the optimum region accounts for 84% of the complete device response, despite the fact that it accounts for 34% of the active device area. It can be seen that the response of the complete device is noticeably less than that of an ideal infinite length electrode array.

Complicating features of this type of resonator design are the different electrode periods in the central grating and the presence of the spacer, which move the device's resonant frequency away from the resonant frequency of the infinite grating. Thus, it is not surprising that the mass sensing behavior of this structure differs from that of an infinite electrode array.

The model suggests that for biosensing applications with a limited quantity of available selective material, to achieve maximum response, this material should only be immobilized over the optimum region of the SAW device. It must be stressed that there are other factors that also need to be taken into account, including analyte transport through the liquid, optimum receptor concentration, and whether a flow through or static cell has been used [25].

On the other hand, in situations such as environmental gas sensing, it is more reasonable to assume that there is an unlimited quantity of analyte interacting with a sensitive layer covering the complete device surface. A comparison of delay line and resonator structures has been made under these assumptions, resulting in quite different conclusions [26].

A limitation of the work presented here is that strong losses have not been considered. These may occur in the case where a viscoelastic guiding layer or sensitive material is used. Also, for biosensing applications, the liquid media are likely to be a conductive buffer solution, which could also induce significant losses, depending on the layer thickness. Acoustic losses will clearly have the effect of reducing the Q factor of the resonance; however, if they occur only at some specific location on the device surface, then they may distort the frequency response and sensitivity distribution.

Although mass sensitivity is investigated here, the mechanism for varying sensitivity across the device surface is not specific to mass loading. The principle is primarily the means by which the device structure translates a local velocity change $\Delta v/v$ to an overall change in the oscillation frequency of the device $\Delta f/f$. Thus, similar results would be expected for sensors based on changes in other parameters such as viscosity or conductivity and for other types of SAW mode.

VI. CONCLUSION

The variation in mass sensitivity across the surface of an SAW resonator sensor has been calculated and verified by experiment. This quantified previous work where it was shown that to achieve a strong response, there is no need to place selective material over the complete device surface. This could be of great economic importance in applications such as biosensing, where the antibodies that are immobilized on the device surface may be very expensive.

Combining an existing Green's function-based analysis with a novel eigen-operator technique, the mechanical interactions between acoustic waves and electrodes buried within layered media have been calculated. It was found that this technique is necessary to achieve good agreement between theory and experiment since the influence of the electrodes confines acoustic energy toward the surface and increases reflection. This approach is much simpler than the FEM-based methods for electrodes buried within layered media and is combined with the COM model to combine the benefits of speed and accuracy.

ACKNOWLEDGMENT

The authors would like to thank the assistance of Prof. A. R. Baghai-Wadji in developing the model for electrodes buried within layered media.

REFERENCES

- [1] D. S. Ballantine, R. M. White, S. J. Martin, A. J. Ricco, E. T. Zellers, G. C. Frye, and H. Wohltjen, *Acoustic Wave Sensors: Theory, Design, and Physico-Chemical Applications*. San Diego, CA: Academic, 1997.
- [2] E. Gizeli, N. J. Goddard, C. R. Lowe, and A. C. Stevenson, "A love plate biosensor utilising a polymer layer," *Sens. Actuators B, Chem.*, vol. 6, no. 1–3, pp. 131–137, Jan. 1992.
- [3] Z. Wang, J. D. N. Cheeke, and C. K. Jen, "Perturbation method for analyzing mass sensitivity of planar multilayer acoustic sensors," *IEEE Trans. Ultrason., Ferroelectr., Freq. Control*, vol. 43, no. 5, pp. 844–851, Sep. 1996.
- [4] G. Kovacs, M. J. Vellekoop, R. Haueis, G. W. Lubking, and A. Venema, "A love wave sensor for (bio)chemical sensing in liquids," *Sens. Actuators A, Phys.*, vol. 43, no. 1–3, pp. 38–43, May 1994.
- [5] J. A. Ogilvy, "The mass-loading sensitivity of acoustic love wave biosensors in air," *J. Phys. D, Appl. Phys.*, vol. 30, no. 17, pp. 2497–2501, 1997.
- [6] D. A. Powell, K. Kalantar-zadeh, and W. Wlodarski, "Comprehensive analysis of SAW sensor performance in liquid media by Green's function method," in *Proc. IEEE Ultrason. Symp.*, Oct. 2003, pp. 146–149.
- [7] G. Watson and E. Staples, "SAW resonators as vapor sensors," in *Proc. IEEE Ultrason. Symp.*, 1990, pp. 311–314.
- [8] G. Watson, W. Horton, and E. Staples, "Gas chromatography utilizing SAW sensors," in *Proc. IEEE Ultrason. Symp.*, 1991, pp. 305–309.
- [9] D. A. Powell, K. Kalantar-zadeh, and W. Wlodarski, "Optimum sensitive area of surface acoustic wave resonator chemical and bio-sensors," in *Proc. IEEE Sensors*, 2005, pp. 1229–1232.
- [10] G. L. Harding, "Mass sensitivity of love-mode acoustic sensors incorporating silicon dioxide and silicon-oxy-fluoride guiding layers," *Sens. Actuators A, Phys.*, vol. 88, no. 1, pp. 20–28, Jan. 2001.

- [11] J. C. Andle, "Final report on SBIR phase II Contract DE-FG02-97ER-81717: Piezoelectric biosensors for bacterial detection and speciation," BIODÉ, Inc., Westbrook, ME, Tech. Rep., 2001.
- [12] R. F. Milsom, N. H. C. Reilly, and M. Redwood, "Analysis of generation and detection of surface and bulk acoustic waves by interdigital transducers," *IEEE Trans. Sonics Ultrason.*, vol. SU-24, no. 3, pp. 147–166, May 1977.
- [13] R. C. Peach, "A general Green function analysis for SAW devices," in *Proc. IEEE Ultrason. Symp.*, 1995, pp. 221–225.
- [14] E. L. Adler, "Matrix methods applied to acoustic waves in multilayers," *IEEE Trans. Ultrason., Ferroelectr., Freq. Control*, vol. 37, no. 6, pp. 485–490, Nov. 1990.
- [15] T. Pasturead, V. Laude, and S. Ballandras, "Stable scattering-matrix method for surface acoustic waves in piezoelectric multilayers," *Appl. Phys. Lett.*, vol. 80, no. 14, pp. 2544–2546, Apr. 2002.
- [16] C. Elachi, "Wave in active and passive periodic structures: A review," *Proc. IEEE*, vol. 64, no. 12, pp. 1666–1698, Dec. 1976.
- [17] V. Plessky and J. Koskela, "Coupling-of-modes analysis of SAW devices," in *Advances in Surface Acoustic Wave Technology, Systems and Applications*, vol. 2, C. C. W. Ruppel and T. A. Fjeldly, Eds. Singapore: World Scientific, 2001, pp. 1–83.
- [18] P. Ventura, J. M. Hodé, J. Desbois, and M. Solal, "Combined FEM and Green's function analysis of periodic SAW structure, application to the calculation of reflection and scattering parameters," *IEEE Trans. Ultrason., Ferroelectr., Freq. Control*, vol. 48, no. 5, pp. 1259–1274, Sep. 2001.
- [19] H. P. Reichinger and A.-R. Baghai-Wadji, "Dynamic 2-D analysis of SAW-devices including massloading," in *Proc. IEEE Ultrason. Symp.*, 1992, pp. 7–10.
- [20] S. Ballandras, V. Laude, T. Pasturead, W. Wilm, W. Daniau, A. Reinhardt, and W. Steichen, "A FEA/BEM approach to simulate complex electrode structures devoted to guided elastic wave periodic transducers," in *Proc. IEEE Ultrason. Symp.*, 2002, pp. 309–312.
- [21] A.-R. Baghai-Wadji, "Theory and applications of Green's functions," in *Advances in Surface Acoustic Wave Technology, Systems and Applications*, vol. 2, C. C. W. Ruppel and T. A. Fjeldly, Eds. Singapore: World Scientific, 2001, pp. 83–149.
- [22] J. Koskela, V. P. Plessky, and M. M. Salomaa, "SAW/LSAW COM parameter extraction from computer experiments with harmonic admittance of a periodic array of electrodes," *IEEE Trans. Ultrason., Ferroelectr., Freq. Control*, vol. 46, no. 4, pp. 806–816, Jul. 1999.
- [23] V. P. Plessky, "A two parameter coupling-of-modes model for shear horizontal type SAW propagation in periodic gratings," in *Proc. IEEE Ultrason. Symp.*, 1993, pp. 195–200.
- [24] D. P. Morgan, "Cascading formulas for identical transducer P-matrices," *IEEE Trans. Ultrason., Ferroelectr., Freq. Control*, vol. 43, no. 5, pp. 985–987, Sep. 1996.
- [25] *Biomolecular Sensors*, E. Gizeli and C. R. Lowe, Eds. London, U.K.: Taylor & Francis, 2002.
- [26] A. Mauder, "SAW gas sensors: Comparison between delay line and two port resonator," *Sens. Actuators B, Chem.*, vol. 26/27, no. 1–3, pp. 187–190, May 1995.



David A. Powell (S'01–M'06) received the Ph.D. degree from the School of Electrical and Computer Engineering, RMIT University, Melbourne, Australia. His thesis is entitled "Modelling of Layered Surface Acoustic Wave Resonators for Liquid Media Sensing Applications."

His interests include chemical and biosensing, microtechnology, acoustic and electromagnetic propagation, periodic media, numerical computing, and novel materials.



Kourosh Kalantar-zadeh (M'94) received the M.Sci. degree in telecommunications from Tehran University, Tehran, Iran, in 1997 and the Ph.D. degree in micro/nano-electronics and bioelectronics from RMIT University, Melbourne, Australia, in 2002.

He is a tenured academic at the School of Electrical and Computer Engineering, RMIT University, Melbourne, Australia. His research interests include chemical and biochemical sensors, nanotechnology, microelectromechanical systems, thermoelectric materials, electronic circuits, and microfluidics. He holds three patents. He has published more than 80 scientific papers in refereed journals and in the proceedings of international conferences. He is currently authoring a book entitled "Nanotechnology Enabled Sensors."



Wojtek Wlodarski (M'72) received the M.Sc.E.E., Ph.D. and D.Sc. degrees, all from the Warsaw University of Technology, Warsaw, Poland, in 1962, 1971, and 1980, respectively.

He has worked in the areas of sensor technology and instrumentation for over 30 years. He is a Professor with RMIT University, Melbourne, Australia, and heads the Sensor Technology Laboratory at the School of Electrical and Computer Engineering. He has published four books and monographs and over 400 papers and holds 29 patents.